Sustainable Energy & Fuels

ROYAL SOCIETY OF CHEMISTRY

PAPER

View Article Online
View Journal | View Issue

Cite this: *Sustainable Energy Fuels*, 2020, **4**, 1180

Stabilization of Li–S batteries with a lean electrolyte *via* ion-exchange trapping of lithium polysulfides using a cationic, polybenzimidazolium binder†

Chuyen Van Pham, *[ab] Lili Liu,[b] Benjamin Britton,[f] Michael Walter, [be] Steven Holdcroft[f] and Simon Thiele *[acd]

Implementing Li–S cells using high S loading and lean electrolyte content is considered the only viable way to achieve competitive specific energy for practical applications. However, under these conditions, the cell cycle life and performance are drastically reduced due to the severe polysulfide shuttle effect, electrolyte depletion, and sluggish electrochemical S conversion. Here we demonstrate that a cationic polymer binder can efficiently mitigate the polysulfide shuttle effect. The employed cationic polymer, poly[2,2′-(2,2″,4,4″,6,6″-hexamethyl-*p*-terphenyl-3,3″-diyl)-5,5′-bibenzimidazolium iodide] (HMT-PMBI(I^-)), possesses abundant benzimidazolium cations which interact with dissolved polysulfide anions when used as an active binder. Simultaneously, density functional theory calculations show that HMT-PMBI$^+$ loosely binds with $TFSI^-$ and Li^+, allowing HMT-PMBI(I^-) to exchange its I^- anion with $TFSI^-$ from the electrolyte salt to form HMT-PMBI(TFSI) containing loosely bound Li^+. This forms a Li^+ conducting phase within the cathode, allowing a reduced electrolyte content. Therefore, the novel active binder enables a stable cyclability of >440 cycles for Li–S batteries with relatively high S-loading (3–4 mg cm^{-2}) and a lean electrolyte content of 6 μl mg_S^{-1}. As the cells prepared in this work use inexpensive, commercially available materials and a conventional doctor-blade fabrication approach, the results are highly relevant to practical applications.

Received 13th November 2019
Accepted 5th December 2019

DOI: 10.1039/c9se01092k

rsc.li/sustainable-energy

1. Introduction

Batteries are nowadays indispensable components in industrial applications such as portable electronic devices and power sources in electric vehicles. Currently, the rechargeable Li-ion battery is the dominant battery type.[1,2] Electrified automobiles are considered the best solution to decrease environmental pollution in the transport sector. To enable the market penetration of electric vehicles, a driving range of at least 500 km is required as well as a further reduction in battery costs. This requires batteries with energy densities of ≥400 W h kg^{-1}, whereas current Li-ion batteries exhibit values of 200–250 W h kg^{-1}, approaching their limit.[3] A promising candidate which meets the above requirements is the Li–S battery, which has a theoretical energy density of ~2600 W h kg^{-1} – which is >four times that of Li-ion cells (~600 W h kg^{-1}).[3] Furthermore, sulfur is abundant, inexpensive, and non-toxic.[3,4] However, the commercialization of Li–S batteries has been obstructed due to their technical deficiencies.[5] These include a short cycle life resulting from the loss of active material caused by the shuttle effect involving the dissolution of higher-order polysulfides (*e.g.*, Li_2S_8, Li_2S_6, and Li_2S_4) in the cell electrolyte. Also, the conversion reactions, $S \rightleftarrows Li_2S$, cause a >75% volume expansion/contraction which leads to their disintegration.[6] The low electrical conductivity (10^{-30} S cm^{-1}) of polysulfur (S_8) and the discharge products (*e.g.* Li_2S and Li_2S_2) further limits both S utilization and battery rate capability.[7] To address these obstacles, Nazar and coworkers[8] introduced the concept of using highly ordered, mesoporous carbon to confine sulfur and polysulfides. These S cathode structures were found to substantially enhance the cycle life and charge capacity and revived the

[a]*Electrochemical Energy Systems, IMTEK – Department of Microsystems Engineering, University of Freiburg, Georges-Koehler-Allee 103, 79110 Freiburg, Germany. E-mail: chuyen.pham@imtek.uni-freiburg.de*

[b]*Institute, Freiburg Center for Interactive Materials and Bioinspired Technologies (FIT), University of Freiburg, Georges-Köhler-Allee 105, 79110 Freiburg, Germany*

[c]*Forschungszentrum Jülich GmbH, Helmholtz-Institute Erlangen-Nürnberg for Renewable Energy (IEK-11), Forschungszentrum Jülich, Egerlandstr. 3, 91058 Erlangen, Germany*

[d]*Department of Chemical and Biological Engineering, Friedrich-Alexander-Universität Erlangen-Nürnberg, Egerlandstr. 3, 91058 Erlangen, Germany. E-mail: si.thiele@fz-juelich.de*

[e]*Fraunhofer IWM, Wöhlerstrasse 11, D-79108 Freiburg i. Br., Germany*

[f]*Department of Chemistry, Simon Fraser University, 8888 University Drive, Burnaby, V5A-1S6, Canada*

† Electronic supplementary information (ESI) available. See DOI: 10.1039/c9se01092k

interest in Li–S battery technology. Since then conductive carbonaceous matrixes have been widely investigated as host materials for sulfur in S-cathodes.[8–12] High cell performances are now achievable with specific capacities approaching theoretical values[13,14] and a cycle life of >1000 cycles.[15,16] Nevertheless, high cell performances have been obtained largely based on low loadings of sulfur (*e.g.*, <2 mg cm^{-2}) and high contents of carbon.[17] Moreover, large amounts of electrolyte per S mass (*e.g.*, E/S > 10 μl mg_S^{-1}, flooded electrolyte) are often used to fill the cathode pores and form percolation pathways for the electrolyte.[18] Based on calculations for a Li–S cell with appropriate parameters, it is noted that the specific energy of Li–S batteries surpasses that of Li-ion analogs only if the electrolyte content is <7 μl mg_S^{-1} and the S-loading is >4 mg cm^{-2}.[19] Unfortunately, conventional Li–S cells usually require an electrolyte content E/S of >10 μl mg_S^{-1} for appropriate electrochemical conversion of S and discharge products, based on the mechanism of dissolution of polysulfides.[20] Due to the low electrical and ion conductivity of S_8, it is necessary that S_8 dissolves in the electrolyte and diffuses to the electron conducting surface, where electrochemical reactions occur at the interface between the host surfaces (electron-conducting phase) and liquid electrolyte (Li^+ conducting phase). Furthermore, the electrolyte is consumed *via* reaction with the Li metal anode during cycling. Therefore, reducing the electrolyte content while maintaining the Li–S cell performance and cyclability with high S-loadings appears to be the only viable way for Li–S batteries to compete with the current Li-ion batteries. Unfortunately, this is the most challenging aspect facing Li–S battery development.[17,21] Yang *et al.*[22] reported the incorporation of MoP nanoparticles in a S-host as the electrocatalyst in order to accelerate the S-conversion kinetics for the Li–S cell using S-loadings of 6 mg cm^{-2} and lean E/S ratios of 4 μl mg_S^{-1}. The cell achieved an areal capacity of ~5 mA h cm^{-2} and 50 cycle durability. Using intercalation–conversion hybrid cathodes of S_8 and Mo_6S_8, Xue *et al.*[23] demonstrated Li–S cells with an E/S ratio of 1.5 μl mg_S^{-1}, delivering a gravimetric energy density of ~400 W h kg^{-1} at the first cycle and at ~300 W h kg^{-1} after approximately 50 cycles at the cell level. Liu and co-workers developed a swellable PEO_{10}LiTFSI polymer gel as a reservoir to trap S_x^{2-}, reporting Li–S cells with E/S ratios of up to 3.3 μl mg_S^{-1} to produce a capacity of 4.6 mA h cm^{-2}. Recently, the strategy of using a large-sized S-host was used to demonstrate Li–S cells with a capacity of ~5 mA h cm^{-2} at the first cycle and of ~3 mA h cm^{-2} after 250 cycles using a S-loading of 5 mg cm^{-2} and E/S of 7 μl mg_S^{-1}.[24] The above are noteworthy developments that focus on lean electrolytes and high S-loadings for Li–S batteries. However, the lean electrolyte conditions exacerbate the instability of Li–S cells; as a result, a satisfactory cycle life has not been realized.

Here, we report the application of a cationic polymer, poly [2,2′-(2,2″,4,4″,6,6″-hexamethyl-*p*-terphenyl-3,3″-diyl)-5,5′-bibenzimidazolium iodide] (HMT-PMBI(I^-)),[25] as an active bifunctional binder for Li–S batteries. On the one hand, the cationic polymer efficiently traps dissolved anionic polysulfides within S cathodes by their interaction with benzimidazolium units of $HMT\text{-}PMBI^+$ as illustrated in Fig. 1. On the other hand, $HMT\text{-}PMBI^+$ loosely binds $TFSI^-$ and Li^+, forming a Li^+ conducting phase within the cathode, allowing for a reduced electrolyte content. The incorporation of HMT-PMBI in Li–S coin cells resulted in a substantially enhanced cycle life compared to that of control cells that incorporate the conventional PVDF binder. The new active binder enables a stable cyclability of >440 cycles for Li–S batteries with relatively high S-loading (3–4 mg cm^{-2}) and a lean electrolyte content of 6 μl mg_S^{-1} using conventional aluminum current collectors. Moreover, this strategy circumvents the use of a traditional polyvinylidene difluoride (PVDF) binder which has a poor affinity for polysulfides and yields mechanically unstable electrodes with high loadings of sulfur.[26]

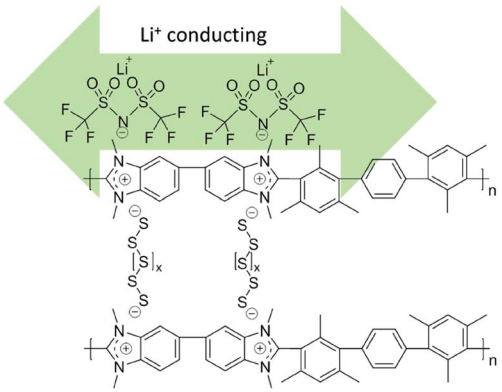

Fig. 1 Schematic illustration of ionic bond formation between polysulfides and $TFSI^-$ anions and benzimidazolium cations and Li^+ conducting percolation.

2. Results and discussion

2.1 Interaction of HMT-PMBI with polysulfides

During the discharge process, polysulfur (S_8) is electrochemically reduced to form lithium polysulfides (Li_2S_x) (x = 1–8). Being polar, high order Li_2S_x (x = 4–8) species dissolve in the electrolyte and escape from the cathode, driven by a concentration gradient. Physical confinement of dissolved Li_2S_x within the carbon matrix in the cathode is inefficient because of the low polarity of the carbon surface. Cationic HMT-PMBI(I^-) contains abundant iodide groups (see Fig. 1) which may exchange with the polysulfides Li_2S_x according to eqn (1).

$$\text{HMT-PMBI}(I^-) + Li_2S_x \rightarrow \text{HMT-PMBI}_{1-z}(S_xLi)_z\downarrow + LiI \quad (1)$$

The presence of I^- in the binder does not affect the cell performance since its redox potential ($I^- \rightleftarrows I_3^-$) is ~3.5 V *versus* Li^+/Li which is outside the electrochemical window of a Li–S cell.[27] This was confirmed by performing cyclic voltammetry (CV) of the Li–S cell using the HMT-PMBI(I^-) binder, and peaks associated with the I^-/I_3^- couple were absent in the CV curve as shown in Fig. 6c. LiI might also play a positive role in stabilization of the solid electrolyte interface (SEI) layers as proved previously.[28] The exchange reaction (1) of Li_2S_x with HMT-PMBI(I^-) was first evidenced in a visual test, where the formation of the HMT-PMBI$(I^-)_{1-z}(S_xLi)_z$ product according to eqn (1)

was observed as follows. When a solution of HMT-PMBI(I^-) in methanol was mixed with a Li_2S_x solution in 1,3-dioxolane/1,2-dimethoxyethane (DOL/DME vol. ratio 1/1) under stirring, the HMT-PMBI(I^-)$_{1-z}$(S_xLi)$_z$ product precipitated and adhered to the wall of the glass vial as shown in Fig. 2. The typical brown color of the Li_2S_x solution disappeared gradually as the HMT-PMBI(I^-)$_{1-z}$(S_xLi)$_z$ compound precipitated. In a control experiment, in which PVDF was added to a solution of Li_2S_x, neither a change in color nor precipitate formation was observed, indicating a weak or no interaction. To collect the HMT-PMBI(I^-)$_{1-z}$(S_xLi)$_z$ product (denoted as HMT-PMBI(S_x)) for further chemical analyses, we conducted the exchange reaction (eqn (1)) with a larger amount of precursors (experimental details are provided in the ESI†). The HMT-PMBI(S_x) that precipitated was filtered and rinsed three times with 50 ml of isopropanol, naturally dried at room temperature, and analyzed using SEM, EDX, Raman, and XPS techniques. The HMT-PMBI(S_x) film exhibited a rough surface, which is significantly different from that of HMT-PMBI(I^-) as shown in Fig. 2c and d, indicating the change in morphology of HMT-PMBI(I^-) upon polysulfide absorption.

The chemical composition of the HMT-PMBI(I^-) film after absorption with Li_2S_x was examined using EDX, XPS, and Raman spectroscopy to elucidate the chemical interaction between them. EDX analysis revealed the chemical composition of pristine HMT-PMBI(I^-) to be 85 at% C, 10 at% N, and 5 at% I. After the Li_2S_x absorption process, the I^- ions of HMT-PMBI(I^-) were replaced by S, resulting in the disappearance of the I peak and the appearance of the S peak (4 at%) in the EDX spectrum of HMT-PMBI(S_x) (Fig. 3a). This supports the proposed counter-ion exchange reaction (eqn (1)) occurring during the absorption process. Since EDX is used to analyze only the surface composition of samples, the extent of replacement of I^- deeper in the sample is unknown.

The absorption of Li_2S_x was further confirmed by the presence of new peaks in the Raman spectrum of HMT-PMBI(S_x) corresponding to different polysulfides, S_3^{2-}, S_4^{2-}, S_5^{2-}, S_6^{2-}, S_7^{2-}, and S_8^{2-},[29] and the absence of such peaks in for the pristine HMT-PMBI(I^-) as shown in Fig. 3b. The XPS study also confirmed the replacement of I atoms with S in HMT-PMBI(S_x), evidenced by the appearance of S(2s) and S(2p) peaks at about 203 eV and 164 eV, respectively, and the vanishing of I(3d) and I(4d) peaks in the spectrum of HMT-PMBI(S_x) as compared to that of HMT-PMBI(I^-) (Fig. 3c). Furthermore, high resolution XPS spectra revealed a shift in the binding energy of the N of HMT-PMBI(S_x) to 404.5 eV relative to 402 eV for benzimidazolium (Fig. 3d).[30] This was attributed to the formation of N–S bonds which increases the binding energy of the N core electrons when compared to the primary N in the benzimidazolium group of HMT-PMBI(I^-). The S(2p) peak is deconvoluted into two peaks at 164 eV and 168 eV, which are ascribed to (–S–S–) of the polysulfide chain and terminal S bound to N of HMT-PMBI(S–N), respectively (Fig. 3e).[31] These experimental results are consistent with density functional theory (DFT) calculations, which show that the binding energy of $[S_xLi_m]^{2-m}$ ($m = 0, 1$) to the HMT-PMBI$^+$ model is stronger than that of $I^{(-)}$ or $TFSI^{(-)}$ as shown in Fig. 4. More details about the most stable configurations of bonding states are available in the ESI (Fig. S1–S3†).

2.2 Incorporation of HMI-PMBI(I^-) in Li–S coin cells

2.2.1 Basic cell characterization. Li–S battery coin cells with S as the active material, Super P carbon as the conductive agent, and HMI-PMBI(I^-) as the binder were prepared. The S/C composite was synthesized by annealing a mixture containing S

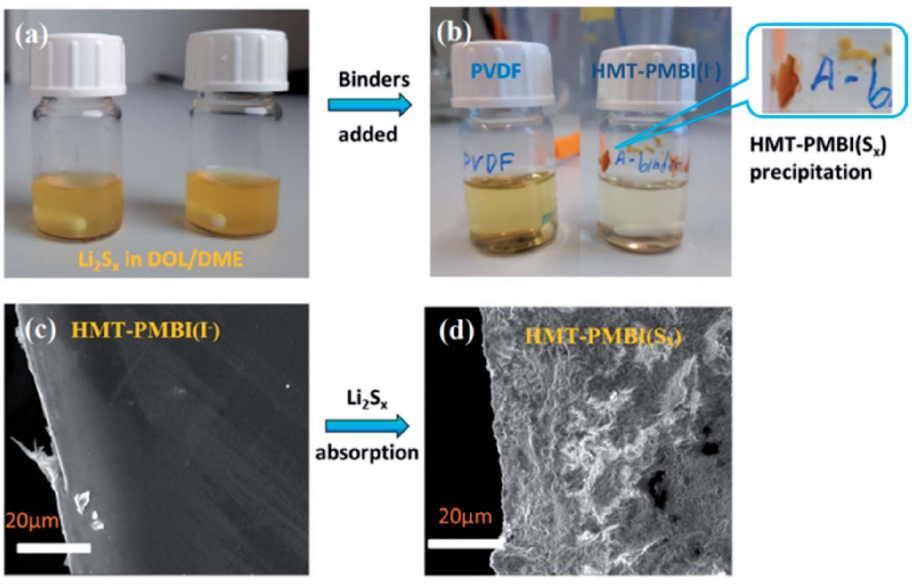

Fig. 2 Visual inspection of the interaction or lack of interaction of the PVDF and HMT-PMBI(I^-) binder with Li_2S_x in solution. (a) Solutions of Li_2S_x in DOL/DME (1 : 1), (b) respective solutions after addition of the PVDF and HMT-PMBI(I^-) binders, respectively, and stirring for 10 min, and a zoomed-in image of the HMT-PMBI(S_x) precipitate in the inset. (c and d) SEM images of a pristine HMI-PMBI(I^-) film and HMT-PMBI(S_x) film, respectively.

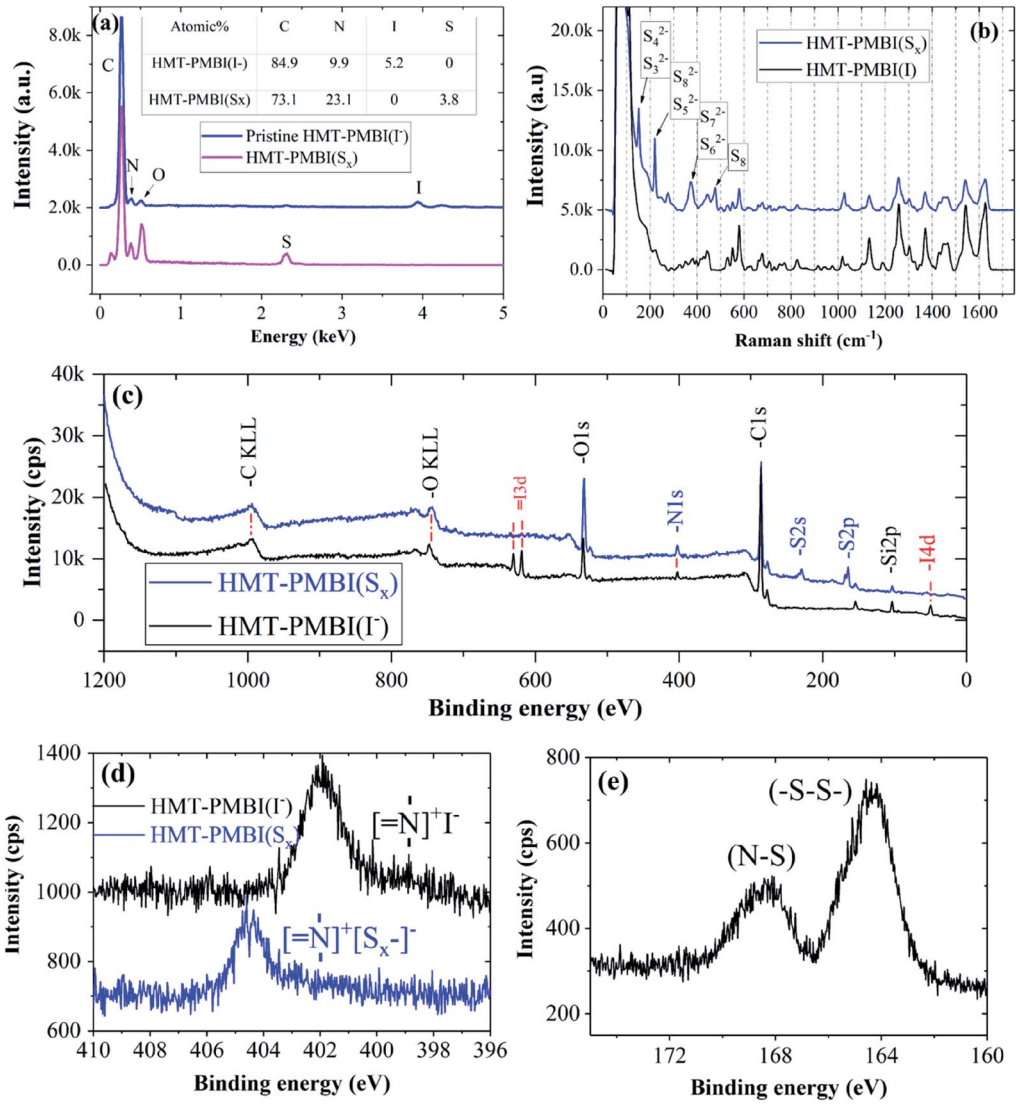

Fig. 3 Spectra of HMI-PMBI(S_x) in comparison with those of pristine HMI-PMBI(I^-): (a) EDX and (b) Raman spectra, (c) overall survey XPS spectra, (d) high resolution scan of the N area, and (e) high resolution scan of the S areas of HMI-PMBI(S_x).

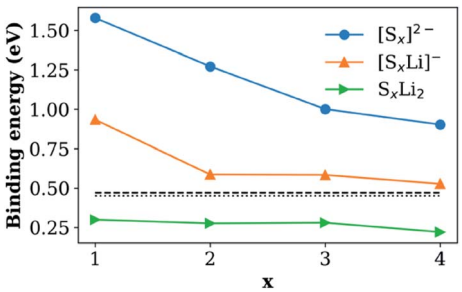

Fig. 4 Binding energy of the HMT-PMBI$^+$ model with $[S_xLi_m]^{2-m}$ species in the presence of the DME/DOL solvent. Dashed and dotted lines show the binding energies of $TFSI^{(-)}$ and $I^{(-)}$ to the HMT-PMBI$^+$ model, respectively.

(70 wt%) and C (30 wt%) at 155 °C in a sealed vial. Under these conditions, S melted and spread on the carbon surface as evidenced in transmission electron microscope (TEM) images, where the S surface (Fig. S4c†) can be distinguished from the carbon surface which has larger crystal lattices (Fig. S4d†). A conventional doctor-blade technique was used to fabricate the cathodes on aluminum foil using ink comprising 80 wt% S/C composite, 10 wt% Super P carbon, and 10 wt% HMT-PMBI(I^-) binder. The prepared cathodes contained 56 wt% S with an areal S loading of about 1.0 mg cm^{-2} and a thickness of ~12 μm as shown in Fig. S4.† Control cells were fabricated with the same parameters using the conventional PVDF binder instead of HMT-PMBI(I^-).

Electrochemical characterization was conducted to examine the proposed function and effect of HMT-PMBI(I^-) on battery performance. During the first discharge/charge at 0.1C (1C = 1675 mA g^{-1}), the HMT-PMBI(I^-) based cell exhibited typical discharge/charge curves with an initial capacity of 1037 mA h g^{-1}, as shown in Fig. 5a. The discharge curve at 0.1C exhibited two voltage plateaus corresponding to two opposite

phase conversion reactions: one at 2.3 V for conversion from solid S_8 to dissolved Li_2S_x ($x = 4$–8) and the other at 2.1 V for conversion from dissolved Li_2S_4 to solid Li_2S_2 or Li_2S.[8,32] The lower voltage plateaus of the cells decreased with the C-rate much faster for the PVDF cell than for the HMT-PMBI(I^-) cell (Fig. 5a, b and d). This indicates more facile Li^+ transport through the HMT-PMBI(I^-) binder layer than through PVDF that resulted in a lower voltage polarization of the HMT-PMBI(I^-) cell compared to the PVDF cell. The cell using the HMT-PMBI(I^-) binder exhibited a good discharge rate capability, indicated by a specific capacity of ~600 mA h g^{-1} at 1C and ~540 mA h g^{-1} at 2C, which are substantially higher than the ~170 mA h g^{-1} at 1C and ~100 mA h g^{-1} at 2C for the control cell (Fig. 5c). This improved discharge rate is attributed to the ionophilicity and wetting properties of the HMT-PMBI(I^-) binder, resulting in faster Li^+ transport within the cathode as compared to that in the cell using ionophobic/non-Li^+ conducting PVDF. It is noted that due to the low wetting ability of PVDF by the electrolyte, the control cell exhibited low capacities at the first two cycles which served as activation steps (Fig. 5c).

Electrochemical impedance spectroscopy (EIS) was performed to investigate the impedances of the two cells at charged states. Nyquist plots of charged HMT-PMBI(I^-) cells at the pristine state, after the first cyclic voltammetry (CV) cycle, and after the first charge/discharge cycle are shown in Fig. 6a. The pristine cell exhibited a single, depressed semicircle and an inclined slope, which are assigned to charge transfer resistance (R_{ct}) and ion transport resistance (Warburg impedance), respectively. The intersection of the EIS curve with the real axis indicates series resistance (R_s) which includes both electrical contact resistance and electrolyte resistance.[33] After cyclic voltammetry and after the first charge/discharge cycle, the EIS spectra exhibited two semicircles, and the total charge transfer resistance decreased. The high frequency arc is attributed to mass transfer resistance through passivated films on both carbon and Li surfaces; the second arc represents charge transfer resistance, which is due to electrochemical reduction of polysulfides at the carbon surface. When comparing the EIS spectra of the HMT-PMBI(I^-) cell with those of the PVDF cell, the HMT-PMBI(I^-) cell exhibited both lower R_s and lower R_{ct} (Fig. 6b) under the same conditions after CV measurements. The lower R_s indicates lower ohmic resistance of the HMT-PMBI(I^-) cell than of the PVDF cell. The lower R_{ct} of the HMT-

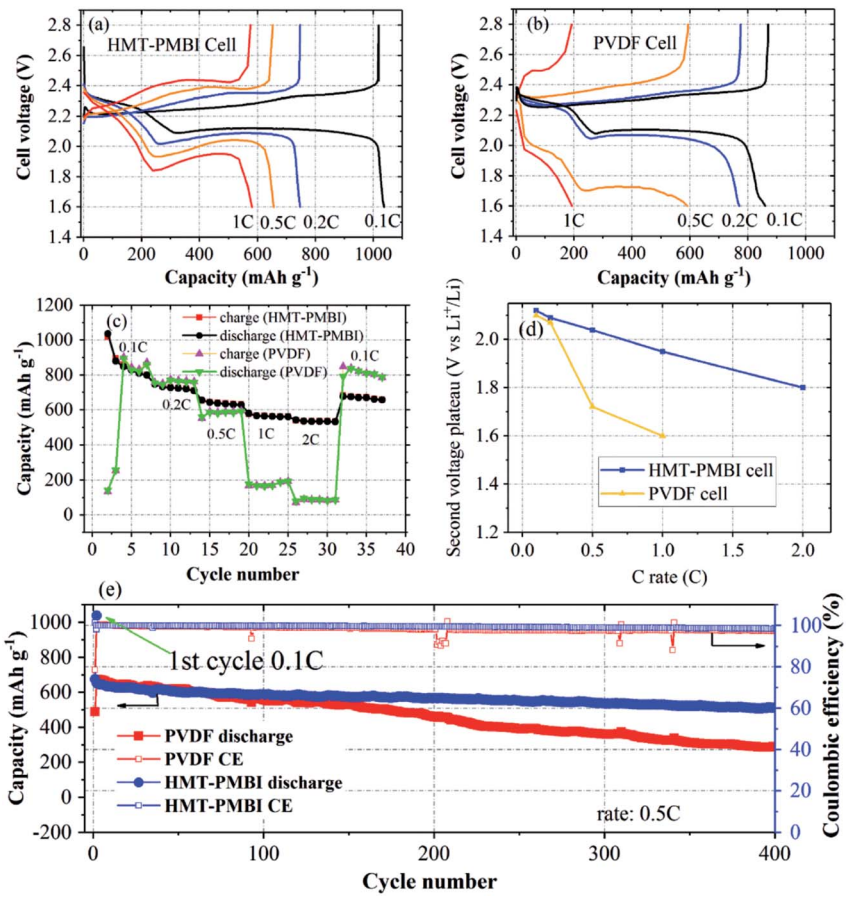

Fig. 5 Characterization of Li–S coin cells. Discharge/charge curves of the cell with the HMT-PMBI(I^-) binder (a) and with the PVDF binder (b). (c) Rate capabilities of cells using the HMT-PMBI(I^-) binder in comparison to a control cell using the PVDF binder. (d) Dependence of the second voltage plateau of discharge curves on the C-rate for the two cells. (e) Charge/discharge cycling of cells with HMT-PMBI(I^-) and PVDF binders after rate capability measurements.

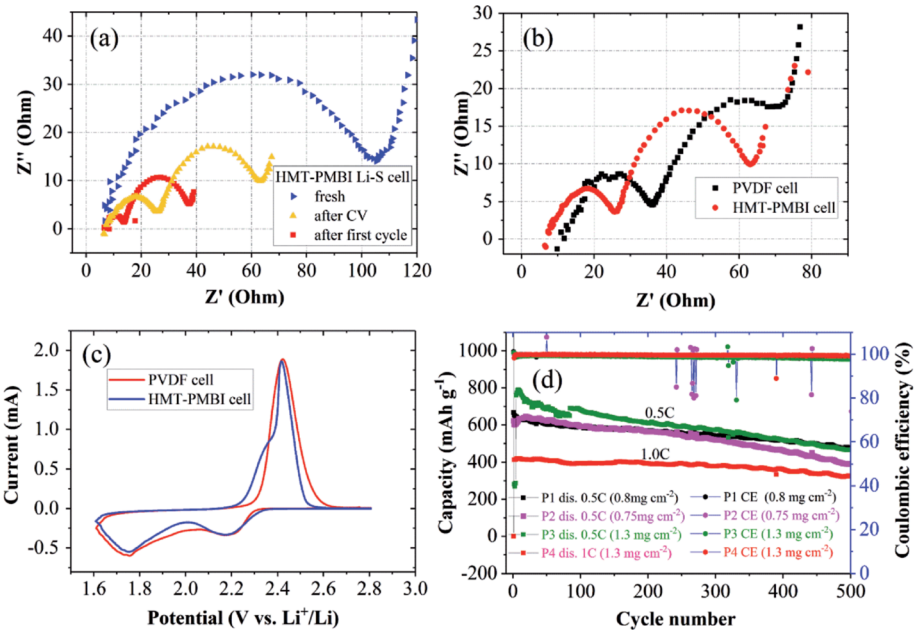

Fig. 6 (a) EIS spectra of the HMT-PMBI(I^-) cell at the pristine state, after CV, and after the first cycle. (b) EIS spectra after CV of the HMT-PMBI(I^-) cell in comparison with the PVDF cell. (c) CV curves of the HMT-PMBI(I^-) cell and PVDF cell. (d) Cycling performances of four cells using the HMT-PMBI(I^-) binder with a S-loading range of 0.75–1.3 mg cm^{-2} at 0.5C (samples P1, P2, and P3) and at 1C (sample P4) for examination of the reproducibility.

PMBI(I^-) cell is ascribed to a lower Li^+ transfer resistance within the HMT-PMBI(I^-) layer compared to PVDF.

CV analysis revealed earlier onset potentials of both S_8/S_8^{2-} reduction and S_x^{2-}/S_8 oxidation peaks (Fig. 6c). These might also be attributed to the enhanced Li^+ ion conductivity of the HMT-PMBI(I^-) binder compared to PVDF as the other factors are the same. This is consistent with the above results from measurements of charge/discharge and rate capability experiments.

The Li^+ ion conductivity of the HMT-PMBI(I^-) polymer can be rationally explained as follows. First, I^- anions are replaced by $TFSI^-$ from the electrolyte. This was confirmed by our DFT results from which we found a slightly better bonding of $TFSI^-$ than $I^{(-)}$ to HMT-PMBI (0.47 eV *vs.* 0.45 eV). The HMT-PMBI($TFSI^-$) forms a quasi-ionic liquid phase along the polymer phase and establishes a Li^+ conducting phase within the polymer. Once S_x^{2-} anions form, they will exchange with $TFSI^-$,[34] again in agreement with our calculations, *c.f.* Fig. 4. When S_x^{2-} is finally reduced to S_8 during the charge process, the binding energy will be 0.05 eV, lower than that of $TFSI^-$ to HMT-$PMBI^+$ (please see Table S1, ESI†). Therefore HMT-$PMBI^+$ will be restored upon binding to $TFSI^-$. This process is reversible upon cycling, maintaining the active function of the HMT-PMBI binder.

Charge/discharge cycles were conducted to examine whether the ability of HMT-PMBI(I^-) to trap polysulfides leads to an improved cycling stability of the cell. The cells were cycled following the rate capability experiments. After 400 cycles at 0.5C, the HMT-PMBI(I^-) cell retained a capacity of 520 mA h g^{-1} against an initial value of 680 mA h g^{-1} corresponding to a degradation rate of 0.059% per cycle. This rate is 2.5 times lower than the 0.146% per cycle for the control PVDF cell which showed a capacity of 284 mA h g^{-1} after 400 cycles at 0.5C (Fig. 5e). The HMT-PMBI(I^-) based cell exhibited a stable coulombic efficiency of ~100% throughout the cycling time. The improved cycling performances provided by the HMT-PMBI(I^-) binder were consistent in multiple cells with S loadings ranging between 0.75 and 1.3 mg cm^{-2}, indicating the reproducibility of these results (as shown in Fig. 6d). At a higher C rate of 1C, the HMT-PMBI(I^-) cell showed a further decrease in the degradation rate to a value of 0.043% per cycle after 500 cycles (Fig. 6d).

2.2.2 Effect of HMI-PMBI(I^-) in high S-loading Li–S coin cells. In an attempt to fabricate more practically relevant S loading cells with the HMT-PMBI(I^-) binder, we used nitrogen-doped carbon nanotubes (N-CNTs) (2.73 at% N, ACS Materials) as S host materials. The morphology and technical parameters of N-CNTs are revealed in the ESI (Table S2 and Fig. S5†). The fiber form of N-CNTs constitutes a better electrical conducting network within the cathodes, decreasing the electrical resistance, which is necessary because cathodes are thicker at high loadings. N-doping improves the kinetics of the electrochemical conversion reaction of S as proven previously.[35] Due to the mechanical flexibility of HMT-PMBI(I^-), structurally robust cathodes with S loadings of ~2–4 mg cm^{-2} were fabricated using a conventional slurry-doctor blade method on C-coated aluminum current collectors. Fig. 7a and b present the cycling performance of a cell with a S-loading of 3.4 mg_S cm^{-2}. The cell exhibited a capacity of 3.3 mA h cm^{-2} at 0.1C (0.60 mA cm^{-2}), corresponding to a specific capacity of 981 mA h g^{-1} of S. This is well above the typical capacity of 2 mA h cm^{-2} for commercial Li-ion batteries.[36] At a discharge rate of 0.2C (1.2 mA cm^{-2}), the

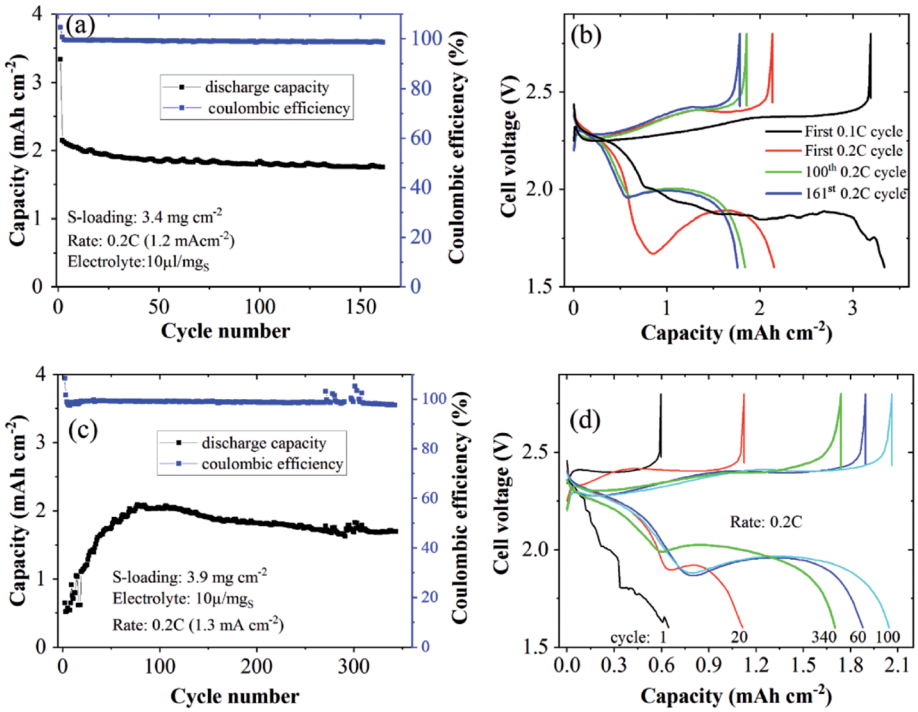

Fig. 7 Cycling performances and discharge/charge curves of Li–S cells using N-CNTs as the S-host and the HMT-PMBI(I^-) binder at S-loadings of 3.4 mg_S cm^{-2} (a and b) and 3.9 mg_S cm^{-2} (c and d).

cell showed a capacity of 2.2 mA h cm^{-2}, which was maintained at 1.8 mA h cm^{-2} after 160 cycles, and exhibited a constant coulombic efficiency of ~100% with continued cycling. These results were consistent in multiple cells having similar loadings (2.9–3.5 mg_S cm^{-2}) (Fig. S6†). For a loading of ~4 mg_S cm^{-2}, a Li–S cell exhibited sluggish electrochemical kinetics, resulting in a low capacity at the beginning of cycle life testing, and required 70 cycles to achieve a peak capacity of 2.1 mA h cm^{-2} at 0.2C. This is the result of the high electrical resistance and poor Li^+ ion transport in thick cathodes, which requires activation of a percolation network *via* redistribution of S within the cathode upon cycling. The cell retained a capacity of 1.7 mA h cm^{-2} after 340 cycles (Fig. 7c and d), which is >80% capacity retention compared to the peak capacity at the 70th cycle after the activation. The coulombic efficiency remained approximately 100% throughout the cycling. In contrast, two control cells using the PVDF binder and NCNT host with S loadings of 2.5 and 3 mg cm^{-2} suffered from a severe shuttle effect at the 151st cycle and the 127th cycle, respectively, and were dysfunctional afterwards (Fig. S7†). A loading of ~4 mg cm^{-2} has been regarded as a critical point for S cathodes using carbon-based hosts on 2D current collectors.[37] Above this loading, conventional S cathodes are often mechanically unstable and have low active-material utilization. To decipher the effect of N-doping on the above samples, we examined Li–S cells using non-doped CNTs with a S-loading of 3.6 mg_S cm^{-2} and the HMT-PMBI(I^-) binder. The cell exhibited a capacity of 1.9 mA h cm^{-2} at 0.1C (0.6 mA cm^{-2}) and retained a 1.2 mA h cm^{-2} capacity after 720 cycles (Fig. S8†). Thus, though the non-doped CNT based cell exhibits a lower capacity at comparable loadings, its stability upon cycling is consistent with that of the N-doped CNT based cell. This observation reaffirms that the HMT-PMBI(I^-) binder is the main reason for the stability of these novel Li–S cells. The high loading cells were tested with an electrolyte content of 10 µl mg_S^{-1}. In an attempt to reduce the electrolyte content, we tested Li–S cells with a S-loading of 2.9 mg cm^{-2} and an electrolyte/S (E/S) ratio of 6 µl mg_S^{-1}. However, this cell delivered a low specific capacity of <300 mA h mg^{-1} due to the sluggish electrochemical kinetics (Fig. S9†), and the cell was dysfunctional after 120 cycles due to the shuttle effect (Fig. S10†).

2.2.3 Modification of the HMT-PMBI(I) binder for Li–S cells with a lean electrolyte content. In typical Li–S cells, due to the low electrical and ion conductivity of S and discharge product Li_2S, the electrochemical reaction occurs only at the interface between the carbon host surfaces (electron-conducting phase) and liquid electrolyte (Li^+ conducting phase). We anticipated that the electrolyte uptake ability and Li^+ conductivity of the HMT-PMBI(I^-) binder could be enhanced by exchanging the I^- counter anions with the $TFSI^-$ of the electrolyte salt. As a result of this, the obtained active HMT-PMBI($TFSI^-$) binder may play the role of the Li^+ conducting phase, and thus the electrolyte content in the cell may be reduced. We first used DFT calculations to determine the applicability of this concept. As mentioned before, the binding energy of $TFSI^-$ to the HMT-$PMBI^+$ model is stronger than that of I^- (Fig. 4), enabling ion exchange to form HMT-PMBI($TFSI^-$). The stable configurations of the binding states are observed in Fig. 8a and b. Li^+ ions still bind to HMT-PMBI(TFSI) with a lower binding energy of 1.26 eV, compared to the 1.79 eV binding energy of Li^+ to $TFSI^-$. These loose bindings of $TFSI^-$ and Li^+ to

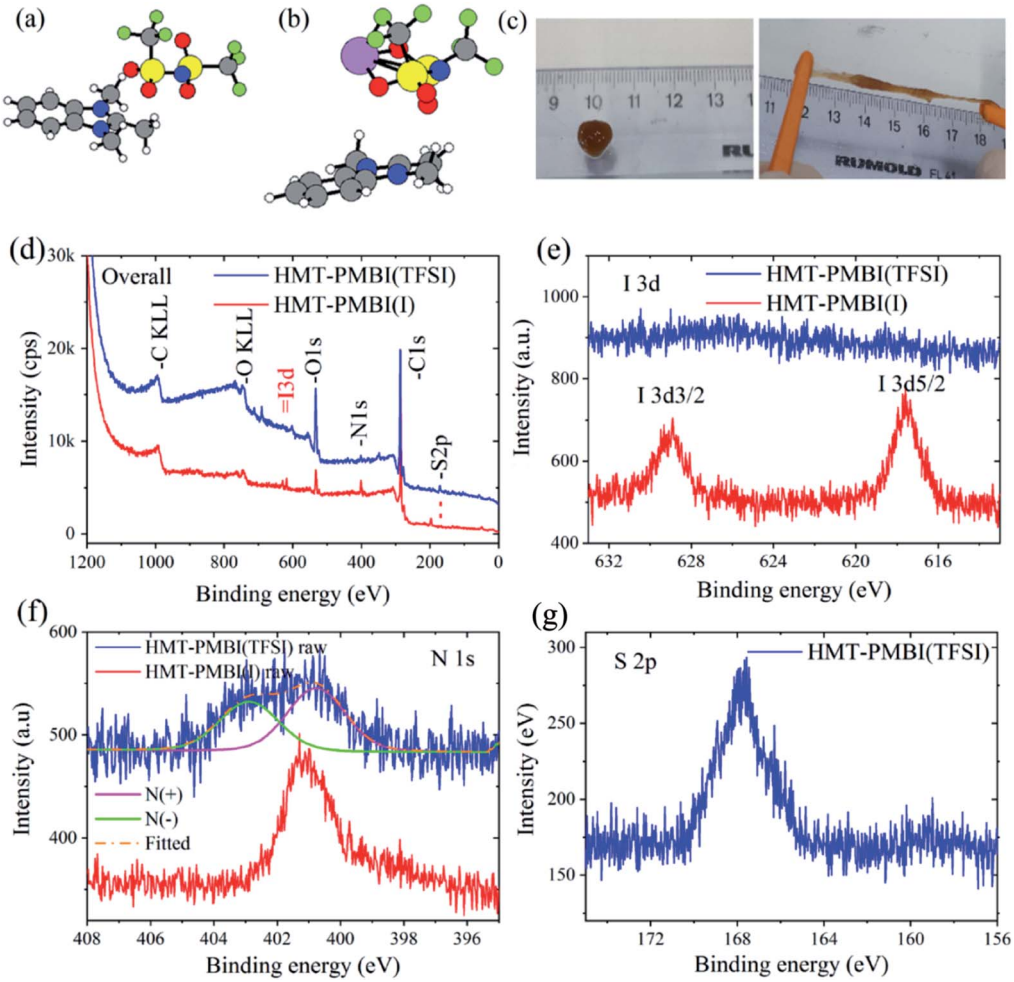

Fig. 8 Lowest energy configurations of (a) HMT-PMBI$^+$ bound to TFSI$^-$ and (b) HMT-PMBI$^+$ bound to LiTFSI. C: grey, H: white, N: blue, S: yellow, O: red, F: green, and Li: purple. (c) Digital images of the HMT-PMBI(TFSI) gel (brown object on the ruler) and its stretchable properties. XPS spectra of HMI-PMBI(TFSI) in comparison with HMI-PMBI(I$^-$): (d) overall survey spectra and (e and f) high resolution scans of the I, N, and S areas.

HMT-PMBI$^+$ might enable the HMT-PMBI polymer to contain movable LiTFSI to form a Li$^+$ ion conducting phase within the cathode. To examine this concept, we first exchanged the I$^-$ counter ion of HMT-PMBI(I$^-$) with the TFSI$^-$ of the electrolyte salt to form HMT-PMBI(TFSI) by stirring HMT-PMBI(I$^-$) in the LiTFSI electrolyte with a DME/DOL solvent for 2 h. The polymer binder did not dissolve but became an amorphous gel with high elasticity (Fig. 8c). It is noted that the DME/DOL solvent was used to simulate the cell environment, whereas for cell fabrication this ion exchange was performed in an *N*-methyl-2-pyrrolidone (NMP) solvent as the first step before cathode slurry preparation (see the Methods). The binding energy order of the species in NMP is TFSI$^-$ > I$^-$, in agreement with that in DME/DOL solvent (Table S1†). In a control experiment, HMT-PMBI(I$^-$) was continuously stirred in the same solvent (DME : DOL 1 : 1) but without the LiTFSI salt. HMT-PMBI(I$^-$) remained a crystalline polymer. Therefore, we rationalize that the anion exchange process changed the HMT-PMBI polymer from the crystal form (HMT-PMBI(I$^-$)) to an amorphous form (HMT-PMBI(TFSI$^-$)). The amorphous form is an essential property for Li$^+$ conduction of gel polymer electrolytes.[38] XPS analyses confirmed the formation of HMT-PMBI(TFSI$^-$) as shown in Fig. 8. The peaks of I(3d) observed in the XPS spectrum of HMT-PMBI(I$^-$) were invisible for HMT-PMBI(TFSI$^-$) (Fig. 8d and e) with the emergence of the S 2p peak at ~168 eV, associated with the sulfonyl S atom of TFSI$^-$ (Fig. 8d and g).[31] This indicates the occurrence of the exchange process of I$^-$ with TFSI$^-$. The N(1s) peak of HMT-PMBI(TFSI$^-$) can be deconvoluted into two components; one at 403 eV attributed to N(−) of TFSI$^-$, and the other at ~401 eV for N(+) of the benzimidazolium group. In contrast, the N(1s) peak of HMT-PMBI(I$^-$) contains only one component at ~401 eV for N(+) (Fig. 8f).

We tested the proposed concept for Li–S batteries incorporated with the HMT-PMBI(TFSI) binder with a S loading of ~3 mg cm^{-2} and a lean electrolyte/S ratio of 6 μl mg$_S^{-1}$. HMT-PMBI(TFSI) comprised 30 wt% LiTFSI with respect to the total mass of HMT-PMBI(I) and LiTFSI. Under the lean electrolyte conditions, the Li–S cell based on HMT-PMBI(TFSI) achieved a specific capacity of 796 mA h g^{-1} (2.4 mA h cm^{-2}) at the first cycle at 0.1C (0.5 mA cm^{-2}). With continued cycling at 0.2C, the

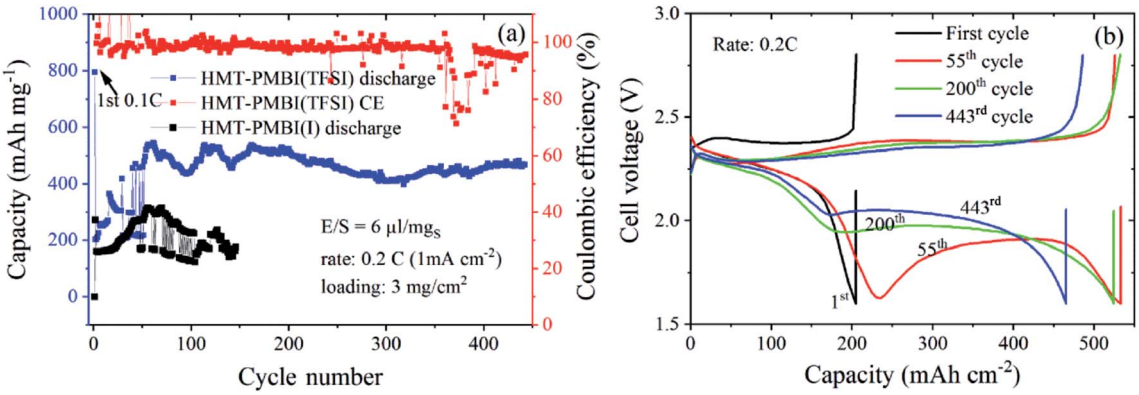

Fig. 9 Cycling performances (a) and discharge/charge curves (b) of Li–S cells using N-CNTs as the S-host and the HMT-PMBI(TFSI) binder at a S-loading of 3 mg$_S$ cm^{-2} and lean E/S of 6 µl mg$_S^{-1}$.

cell required 50 conditioning cycles to be fully activated, exhibiting a stable specific capacity of 450–500 mA h g^{-1} (1.35–1.5 mA h cm^{-2}) over 440 cycles (Fig. 9a). The coulombic efficiency of the cell was ~99 ± 1%, but it suffered a fluctuation after 360 cycles, which might be due to the instability of the Li metal anode. This cell exhibited a typical discharge and charge voltage profile after cell conditioning (Fig. 9b). In contrast, while employing a lean E/S ratio, the HMT-PMBI(I) based cell delivered a low specific capacity of <300 mA h mg^{-1} and was dysfunctional after 120 cycles due to the shuttle effect as mentioned above (Fig. 9, S9 and S10†). The cell failure can be explained as follows. At the end of the upper voltage plateau, the concentration of dissolved Li_2S_x was maximal, which severely increased the viscosity of the electrolyte under lean conditions. This led to dramatically reduced Li^+ conductivity, resulting in high voltage polarization and the loss of the second voltage plateau (Fig. S9†). However, the presence of Li^+ and $TFSI^-$ loosely bound in the HMT-PMBI(TFSI) matrix enhanced the electrolyte uptake and Li^+ conductivity. This facilitates appropriate electrochemical conversion of S under lean electrolyte conditions. As a result, the second voltage plateau of this cell was observed (Fig. 9b).

A gravimetric energy density of 172 kW h kg^{-1} was estimated for this Li–S cell using the capacity of the first cycle at 0.1C at the system level, considering the mass of the current collector, cathode, electrolyte, separator, and a simulated Li anode with a thickness of 50 µm (see Table S3† for the detailed parameters used for the energy density calculation). Although this energy density is moderate, the cycle life of the Li–S battery in this work is outstanding for Li–S batteries using 2D current collectors under lean electrolyte conditions (*i.e.*, E/S < 7 µl mg$_S^{-1}$) and with a S-loading ≥3 mg cm^{-2} (Table S4†). The S-loadings employed in this work are lower than those achieved with the usage of 3D carbon based current collectors.[39,40] However, the research community has recognized that 3D current collector cells might not be feasible for practical applications since their designs greatly differ from standard Li-ion battery configurations.[24] In addition, 3D current collector configurations might require a large amount of the electrolyte, and electrode-tab welding and the high cost of carbon fiber mats are amongst other concerns. Therefore, the interesting results of Li–S cells with 2D current collectors achieved by the introduction of the novel active binder HMT-PMBI(TFSI) are promising. Still, the energy density of Li–S batteries at the cell level achieved in this work is inferior to that of the state-of-the-art Li-ion counterparts. Further optimization of cathode morphology using this binder concept in Li–S cells might even further reduce the electrolyte content and increase S loading and utilization, and could lead to practically viable Li–S batteries.

3. Conclusion

HMT-PMBI(I^-) is demonstrated to serve as an active binder that also traps polysulfides within the cathodes of Li–S batteries by forming ionic interactions with dissolved polysulfide anions. This leads to a significantly improved cycling performance of the S cathode comprising sulfur, Super P carbon, and the HMT-PMBI(I^-) binder as compared to the cathode using a conventional PVDF binder. The new cathode exhibited an initial capacity of 1037 mA h g^{-1} at 0.1C (62% S utilization) which is similar to that of the control cathode using PVDF. However, at a high discharge rate ≥1C, the HMT-PMBI(I^-) cell exhibited a much higher capacity compared with the PVDF-based cell due to a higher rate capability resulting from the improved wetting of the cathode and enhanced Li^+ conductivity. The HMT-PMBI(I^-) binder in combination with N-doped CNTs as the S-host facilitates the fabrication and proper operation of high S-loading Li–S batteries, which have an areal capacity comparable with that of commercial Li-ion batteries. Density functional theory calculation shows that HMT-$PMBI^+$ loosely binds with $TFSI^-$ and Li^+. As a result, HMT-PMBI(I^-) can exchange its I^- anion with $TFSI^-$ to form HMT-PMBI(TFSI) containing loosely bound Li^+. This acts as the Li^+ conducting phase within the cathode, allowing a reduced electrolyte content in the Li–S cell. Therefore, the new active binder enables a stable cyclability of >440 cycles for Li–S batteries with a relatively high S-loading (3–4 mg cm^{-2}) and a lean electrolyte content of 6 µl mg$_S^{-1}$. Although the specific energy density of this Li–S cell is moderate, to our knowledge this is one of the few most outstanding cyclabilities reported to date for Li–S batteries

under lean electrolyte conditions and relatively high loadings. We suggest that integration of this new binder with other advanced components, *e.g.* electrolyte, anode, and host materials, could result in further improved performance of Li–S batteries. As this work uses all inexpensive, commercially available materials and conventional battery fabrication, the results are highly relevant to practical applications. HMT-PMBI(I^-) can also be applicable as a new binder for other battery types such as Li-ion batteries.

4. Methods

4.1 Electrochemical characterization

The sulfur/carbon composite was prepared by first grinding carbon (Super P) and S powder in a vial using a stir bar for 12 h. The obtained S/C composite (70 wt% S) was further annealed at 155 °C in a sealed vial. The final S content was 68 wt% which was calculated from the weight of the final composite. The cathode slurry was fabricated by stirring a mixture of 80 wt% S/C composite, 10 wt% Super P carbon, and 10 wt% HMT-PMBI(I^-) binder (Ionomr Innovations Inc) in *N*-methy1-2-pyrrolidone in a vial on a magnetic stir plate at room temperature overnight. S cathodes were prepared by coating the slurry on a carbon-coated aluminum foil current collector using the doctor-blade coating technique, followed by drying in a vacuum oven at 60 °C for 12 h. For coin cell assembly, the sulfur electrodes were cut into discs with a diameter of 11.1 mm, corresponding to the geometric disc area of 0.97 cm^2. The sulfur loading was about 1.0 mg cm^{-2} for carbon black based electrodes. The electrolyte was a solution of 1.0 M lithium bis-trifluoromethane sulfonylimide (LiTFSI) and 0.2 M $LiNO_3$ additive in a mixed solvent of 1,3-dioxolane (DOL) and 1,2-dimethoxyethane (DME) with a volume ratio of 1 : 1. An electrolyte dose corresponding to 15 μl mg_S^{-1} was used for the basic cell tests. Li chips with a diameter of 15.6 mm and a thickness of 0.45 mm were used as the counter electrodes. Coin cells (CR2032) were assembled in an Ar-filled glove box with Celgard PP separators (25 μm thick). The rate capability and cycling performance were analyzed using a Landt CT2001A-5V 5 mA battery tester between 1.6 and 2.8 V at various current densities. High loading S/NCNT based coin cells were prepared and tested in the same manner as described above except for the following. The S content in the S/NCNT composite was 75 wt%, the electrolyte content was 10 μl mg_S^{-1}, an ink mixture of 75 wt% S/NCNT composite, 15 wt% Super P carbon, and 10 wt% HMT-PMBI(I^-) binder was used, and the S loadings were 2–4 mg cm^{-2}. NCNTs were purchased from ACS Materials with detailed parameters available in the ESI.† For the lean electrolyte tests, HMT-PMBI(TFSI) Li–S coin cells with a lean electrolyte were fabricated using the same procedure as that for the HMT-PMBI(I^-) based cells except that during the first step of slurry preparation, the I^- anion of HMT-PMBI(I) was exchanged with $TFSI^-$. In particular, HMT-PMBI(I^-) and LiTFSI with a 7 : 3 wt ratio were added to the NMP solution and continuously stirred for 2 h before S/NCNTs and Super P carbon were added. The same electrolyte was used but with a dosage corresponding to 6 μl mg_S^{-1}. CV tests were performed at a scan rate of 0.1 mV s^{-1} in a potential window of 1.6–2.8 V (*vs.* Li/Li^+) and EIS measurements were conducted in the frequency range from 0.1 to 10^5 Hz at a constant perturbation amplitude of 5 mV on an ECi-200 potentiostat (Nordic Electrochemistry).

4.2 Simulation

Density functional theory (DFT) calculations were performed with the GPAW package,[41,42] where the electron density and the Kohn–Sham wave functions are represented using the PAW formalism.[43] The smooth wave functions were represented on real space grids with a grid spacing of 0.2 Å. Exchange and correlation energies were approximated as devised by Perdew, Burke and Ernzerhof (PBE).[44] Solvent effects are considered by using the average value of $\varepsilon = 7.27$ for DME and DOL.[45]

The HMT-PMBI polymer was modeled using the 1,2,3-trimethyl 1*H*-benzimidazolium cation as shown in Fig. 8a. Bonded structures were created by placing the molecules in random relative orientations resulting in at least 150 configurations for each pairing. These were allowed to relax without symmetry restrictions until all forces were found to be below 0.05 eV $Å^{-1}$. The energetically lowest structure was used to obtain the binding energy.

Conflicts of interest

Polybenzimidazolium AEM technology is licensed by Simon Fraser University to Ionomr Innovations Inc. Steven Holdcroft and Benjamin Britton are co-founders and minor shareholders of Ionomr Innovations Inc. The authors declare no conflicting interests.

Acknowledgements

This work was financed by the Deutsche Forschungsgemeinschaft (DFG) under project number 389154849. We thank Thomas Böhm for Raman spectra measurements.

References

1 H.-G. Jung, M. W. Jang, J. Hassoun, Y.-K. Sun and B. Scrosati, *Nat. Commun.*, 2011, **2**, 516.
2 M. Armand and J.-M. Tarascon, *Nature*, 2008, **451**(7179), 652.
3 P. G. Bruce, S. A. Freunberger, L. J. Hardwick and J.-M. Tarascon, *Nat. Mater.*, 2012, **11**(1), 19.
4 Y. Yang, G. Zheng and Y. Cui, *Chem. Soc. Rev.*, 2013, **42**(7), 3018.
5 X. Fang and H. Peng, *Small*, 2015, **11**(13), 1488.
6 S. Waluś, C. Barchasz, J.-F. Colin, J.-F. Martin, E. Elkaïm, J.-C. Leprêtre and F. Alloin, *Chem. Commun.*, 2013, **49**(72), 7899.
7 A. Manthiram, Y. Fu, S.-H. Chung, C. Zu and Y.-S. Su, *Chem. Rev.*, 2014, **114**(23), 11751.
8 X. Ji, K. T. Lee and L. F. Nazar, *Nat. Mater.*, 2009, **8**(6), 500.
9 L. Ji, M. Rao, H. Zheng, L. Zhang, Y. Li, W. Duan, J. Guo, E. J. Cairns and Y. Zhang, *J. Am. Ceram. Soc.*, 2011, **133**(46), 18522.

10 G. He, X. Ji and L. Nazar, *Energy Environ. Sci.*, 2011, **4**(8), 2878.
11 X. Ji, S. Evers, R. Black and L. F. Nazar, *Nat. Commun.*, 2011, **2**, 325.
12 N. Jayaprakash, J. Shen, S. S. Moganty, A. Corona and L. A. Archer, *Angew. Chem., Int. Ed.*, 2011, **50**(26), 5904.
13 S. Xin, L. Gu, N.-H. Zhao, Y.-X. Yin, L.-J. Zhou, Y.-G. Guo and L.-J. Wan, *J. Am. Ceram. Soc.*, 2012, **134**(45), 18510.
14 H.-J. Peng, J. Liang, L. Zhu, J.-Q. Huang, X.-B. Cheng, X. Guo, W. Ding, W. Zhu and Q. Zhang, *ACS Nano*, 2014, **8**(11), 11280.
15 G. Li, W. Lei, D. Luo, Y.-P. Deng, D. Wang and Z. Chen, *Adv. Energy Mater.*, 2017, **498**, 1702381.
16 M. Liu, Q. Meng, Z. Yang, X. Zhao and T. Liu, *Chem. Commun.*, 2018, **54**, 5090.
17 S.-H. Chung, C.-H. Chang and A. Manthiram, *Adv. Funct. Mater.*, 2018, **114**, 1801188.
18 X. Yang, X. Li, K. Adair, H. Zhang and X. Sun, *Electrochem. Energy Rev.*, 2018, **2**(44), 76.
19 M. Hagen, D. Hanselmann, K. Ahlbrecht, R. Maça, D. Gerber and J. Tübke, *Adv. Energy Mater.*, 2015, **5**(16), 1401986.
20 H. Pan, K. S. Han, M. H. Engelhard, R. Cao, J. Chen, J.-G. Zhang, K. T. Mueller, Y. Shao and J. Liu, *Adv. Funct. Mater.*, 2018, **8**, 1707234.
21 R. Fang, S. Zhao, Z. Sun, D.-W. Wang, H.-M. Cheng and F. Li, *Adv. Mater.*, 2017, **29**, 1606823.
22 Y. Yang, Y. Zhong, Q. Shi, Z. Wang, K. Sun and H. Wang, *Angew. Chem.*, 2018, **57**(47), 15549.
23 W. Xue, Z. Shi, L. Suo, C. Wang, Z. Wang, H. Wang, K. P. So, A. Maurano, D. Yu, Y. Chen, L. Qie, Z. Zhu, G. Xu, J. Kong and J. Li, *Nat. Energy*, 2019, **29**, 1601759.
24 M. Li, Y. Zhang, Z. Bai, W. W. Liu, T. Liu, J. Gim, G. Jiang, Y. Yuan, D. Luo, K. Feng, R. S. Yassar, X. Wang, Z. Chen and J. Lu, *Adv. Mater.*, 2018, **30**(46), e1804271.
25 A. G. Wright, J. Fan, B. Britton, T. Weissbach, H.-F. Lee, E. A. Kitching, T. J. Peckham and S. Holdcroft, *Energy Environ. Sci.*, 2016, **9**(6), 2130.
26 J. Liu, Q. Zhang and Y.-K. Sun, *J. Power Sources*, 2018, **396**, 19.
27 Y. Zhao, M. Hong, N. Bonnet Mercier, G. Yu, H. C. Choi and H. R. Byon, *Nano Lett.*, 2014, **14**(2), 1085.
28 F. Wu, J. T. Lee, N. Nitta, H. Kim, O. Borodin and G. Yushin, *Adv. Mater.*, 2015, **27**(1), 101.
29 M. Hagen, P. Schiffels, M. Hammer, S. Dorfler, J. Tubke, M. J. Hoffmann, H. Althues and S. Kaskel, *J. Electrochem. Soc.*, 2013, **160**(8), A1205–A1214.
30 C.-Y. Chen, H.-J. Peng, T.-Z. Hou, P.-Y. Zhai, B.-Q. Li, C. Tang, W. Zhu, J.-Q. Huang and Q. Zhang, *Adv. Mater.*, 2017, **29**, 1606802.
31 https://srdata.nist.gov/xps/Default.aspx, last accessed June 2018.
32 S. S. Zhang, *Electrochim. Acta*, 2012, **70**, 344.
33 N. A. Cañas, K. Hirose, B. Pascucci, N. Wagner, K. A. Friedrich and R. Hiesgen, *Electrochim. Acta*, 2013, **97**, 42.
34 L. Li, T. A. Pascal, J. G. Connell, F. Y. Fan, S. M. Meckler, L. Ma, Y.-M. Chiang, D. Prendergast and B. A. Helms, *Nat. Commun.*, 2017, **8**(1), 2277.
35 H.-J. Peng, T.-Z. Hou, Q. Zhang, J.-Q. Huang, X.-B. Cheng, M.-Q. Guo, Z. Yuan, L.-Y. He and F. Wei, *Adv. Mater. Interfaces*, 2014, **1**(7), 1400227.
36 J. Xiao, *Adv. Energy Mater.*, 2015, **5**(16), 1501102.
37 D. Lv, J. Zheng, Q. Li, X. Xie, S. Ferrara, Z. Nie, L. B. Mehdi, N. D. Browning, J.-G. Zhang, G. L. Graff, J. Liu and J. Xiao, *Adv. Energy Mater.*, 2015, **5**(16), 1402290.
38 D. Lei, K. Shi, H. Ye, Z. Wan, Y. Wang, L. Shen, B. Li, Q.-H. Yang, F. Kang and Y.-b. He, *Adv. Funct. Mater.*, 2018, **28**(38), 1707570.
39 S.-H. Chung and A. Manthiram, *Adv. Mater.*, 2018, **30**, 1705951.
40 S.-H. Chung and A. Manthiram, *Joule*, 2018, **2**, 1–15.
41 J. J. Mortensen, L. B. Hansen and K. W. Jacobsen, *Phys. Rev. B: Condens. Matter Mater. Phys.*, 2005, **71**(3), 4351.
42 J. Enkovaara, C. Rostgaard, J. J. Mortensen, J. Chen, M. Dułak, L. Ferrighi, J. Gavnholt, C. Glinsvad, V. Haikola, H. A. Hansen, H. H. Kristoffersen, M. Kuisma, A. H. Larsen, L. Lehtovaara, M. Ljungberg, O. Lopez-Acevedo, P. G. Moses, J. Ojanen, T. Olsen, V. Petzold, N. A. Romero, J. Stausholm-Møller, M. Strange, G. A. Tritsaris, M. Vanin, M. Walter, B. Hammer, H. Häkkinen, G. K. H. Madsen, R. M. Nieminen, J. K. Nørskov, M. Puska, T. T. Rantala, J. Schiøtz, K. S. Thygesen and K. W. Jacobsen, *J. Phys.: Condens. Matter*, 2010, **22**(25), 253202.
43 P. E. Blochl, *Phys. Rev. B: Condens. Matter Mater. Phys.*, 1994, **50**(24), 17953.
44 J. P. Perdew, K. Burke and M. Ernzerhof, *Phys. Rev. Lett.*, 1996, **77**(18), 3865.
45 A. Held and M. Walter, *J. Chem. Phys.*, 2014, **141**(17), 174108.

